

A Narrow Uniform Core with a Wide Structured Wing: Modeling the TeV and Multi-wavelength Afterglows of GRB 221009A

JIAN-HE ZHENG,^{1,2} XIANG-YU WANG,^{1,2} RUO-YU LIU,^{1,2} AND BING ZHANG^{3,4}

¹*School of Astronomy and Space Science, Nanjing University, Nanjing 210023, People's Republic of China*

²*Key laboratory of Modern Astronomy and Astrophysics (Nanjing University),
Ministry of Education, Nanjing 210023, People's Republic of China*

³*Nevada Center for Astrophysics, University of Nevada Las Vegas, Las Vegas, NV 89154, USA*

⁴*Department of Physics and Astronomy, University of Nevada Las Vegas, Las Vegas, NV 89154, USA*

ABSTRACT

The TeV afterglow of the BOAT GRB 221009A was interpreted as arising from a narrow jet while the radio to X-ray afterglows were interpreted as arising from a wide structured jet. However, there is no model explaining the TeV and lower-energy multi-wavelength afterglows simultaneously. We here investigate a two-component jet model, including a narrow uniform core with a wide structured wing, to explain both the multi-wavelength afterglows that last up to 100 days. We find that to explain the early TeV afterglow with the inverse-Compton process, we need a circum-burst density higher than $\gtrsim 0.1\text{cm}^{-3}$, while the radio afterglow and the H.E.S.S. upper limit combine to constrain the density to be lower at larger radii. Thus, a decreasing density profile with radius is favored. Considering that the rising TeV light curve during the afterglow onset favors a constant-density medium, we invoke a stratified density profile, including a constant-density profile at small radii and a wind density profile at large radii. We find that the two-component jet model with such a stratified density profile can explain the TeV, X-ray and optical afterglows of GRB 221009A, although the radio fluxes exceed the observed ones by a factor of two at later epochs. The discrepancy in the radio afterglow could be resolved by invoking some non-standard assumption about the microphysics of afterglow shocks. The total kinetic energy of the two components in our model is $\lesssim 10^{52}\text{erg}$, significantly smaller than that in the single structured jet models.

Keywords: Gamma-ray burst (629) — Gamma-ray astronomy (628) — High energy astrophysics (739)

1. INTRODUCTION

GRB 221009A is the brightest-of-all-time (BOAT) GRB (Burns et al. 2023). Due to its enormous energy ($E_{\gamma,\text{iso}} = 1.5 \times 10^{55}$ erg) (An et al. 2023; Lesage et al. 2023) and proximity ($z = 0.151$) (Castro-Tirado et al. 2022), GRB 221009A is an exceptionally rare event (O'Connor et al. 2023; Burns et al. 2023; Williams et al. 2023). The Large High Altitude Air Shower Observatory (LHAASO) observed GRB 221009A at the earliest epoch, covering both the prompt emission phase and the early afterglow in TeV band, and

revealed the onset of afterglow emission in the TeV band for the first time (LHAASO Collaboration 2023).

In addition, the temporal slope of the TeV light curve in the decaying phase steepens from $\alpha = -1.12_{-0.01}^{+0.01}$ to $\alpha = -2.21_{-0.83}^{+0.30}$ at $t_b = 670_{-110}^{+230}\text{s}$ after the afterglow onset time $T^* = T_0 + 226\text{s}$, where T_0 is the trigger time of this GRB¹, indicating that the opening angle of the jet of GRB 221009A is only $\sim 0.8^\circ$ (LHAASO Collaboration 2023). This reduces the beaming-corrected energy in gamma-rays to a level of $10^{50} - 10^{51}\text{erg}$ for GRB 221009A, which agrees with the beaming-corrected gamma-ray energy release in other GRBs (Frail et al. 2001).

xywang@nju.edu.cn

¹ We note $F_\nu \propto \nu^\beta t^\alpha$ throughout this paper

It has been suggested that jets of GRBs may not be uniform, but characterized by a significant anisotropy of the angular distribution of the fireball energy around the axis (Rossi et al. 2002; Zhang & Mészáros 2002). In the assumption of a structured jet model, the small half opening angle of GRB 221009A implies a narrow core component, which is only responsible for the early afterglow emission before 10^4 s (LHAASO Collaboration 2023), while the late-time ($> 10^4$ s) afterglow emission may require other jet components.

The X-ray afterglow of GRB 221009A features an initial power-law decay index of $\alpha_1 = -1.52 \pm 0.01$, steepening to $\alpha_2 = -1.66 \pm 0.01$ after 0.82 ± 0.07 days after the trigger, which is not consistent with standard predictions for the emission from a top-hat jet (O’Connor et al. 2023; Williams et al. 2023). O’Connor et al. (2023) interpreted the X-ray afterglow as due to a structured jet expanding into a constant-density medium, where the jet is composed by an inner component of angular size θ_b with a shallow energy profile $dE/d\Omega \propto \theta^{-a_1}$ and slightly steeper lateral structure at $\theta > \theta_b$ with $dE/d\Omega \propto \theta^{-a_2}$ ($a_2 > a_1$). Gill & Granot (2023) also explored a structured jet model to explain the multi-wavelength afterglow of GRB 221009A, but assuming a wind density profile for the surrounding medium. In both models, the early radio emission is attributed to electrons accelerated by the reverse shock, while the optical and X-ray afterglows, as well as the late radio afterglow, arise from the forward shock. A two-component jet model consisting of a narrow top-hat jet and a broader top-hat jet has been proposed to explain the multi-wavelength data from radio to GeV afterglows of GRB 221009A (Sato et al. 2023). Besides the two-component jet models, various other types of models were also proposed to explain the multi-wavelength data of GRB 221009A (Ren et al. 2023; Zhang et al. 2023).

The above models, however, did not take into account the early TeV data observed by LHAASO, which were not available at that time. In this work, we explore a two-component jet model, including a narrow top-hat jet (core) and a wider wing with an angular structure, to explain both the TeV afterglow measured by LHAASO and lower energy multi-wavelength afterglows of GRB 221009A.

2. THE SET-UP OF A TWO-COMPONENT JET MODEL

The afterglow of GRB 22109A exhibits two breaks in light curves. The early sharp break in the TeV band is consistent with a jet break from a top hat jet (LHAASO Collaboration 2023), while the later shallow break could be due to the change of the angular profile

$dE/d\Omega \propto \theta^{-a}$ of a structured jet (O’Connor et al. 2023; Gill & Granot 2023). This complex behaviour suggests a jet composing of a inner, narrow top-hat core component and a outer, wide wing component with an angular structure, which can be described by (Zhang et al. 2024)

$$\epsilon \equiv \frac{dE}{d\Omega} = \begin{cases} \epsilon_I, & \theta < \theta_j, \\ \epsilon_{II}f(\theta), & \theta_j < \theta < \Theta, \end{cases} \quad (1)$$

where θ_j is the opening angle of the narrow core, Θ is the maximum angle of the structured wing, and $f(\theta)$ is the structure function of the wing. The isotropic energy of the wing could be much smaller than that of the core ($\epsilon_I \gg \epsilon_{II}$), which can only be determined by the afterglow data. We assume a smooth broken power-law function for the structure of the wing, as given by (Granot & Kumar 2003)

$$f(\theta) = \left[\left(\frac{\theta}{\theta_{c,w}} \right)^{2a_1} + \left(\frac{\theta}{\theta_{c,w}} \right)^{2a_2} \right]^{-1/2}, \quad (2)$$

where $\theta_{c,w}$ is the transition angle from a shallow angular profile to a steeper ($a_2 > a_1$) angular profile of the wide wing. The structured function declines as $f(\theta) \propto \theta^{-a_1}$ from θ_j to $\theta_{c,w}$ and then transfers into $f(\theta) \propto \theta^{-a_2}$ after $\theta_{c,w}$. The shallow jet break happens when the observers see the edge of $\theta_{c,w}$.

Correspondingly, one could also define a jet structure of the angle-dependent initial Lorentz factor, i.e.

$$\Gamma_0(\theta) = \begin{cases} \Gamma_{I,0}, & \theta < \theta_j \\ \Gamma_{II,0}g(\theta), & \theta_j < \theta < \Theta, \end{cases} \quad (3)$$

where $\Gamma_{I,0} \gg \Gamma_{II,0}$ and $g(\theta)$ is the structure function of the Lorentz factor profile.

The narrow jet core could be a Poynting-flux dominated jet (Dai et al. 2023; Yang et al. 2023) and the wide wing could be matter-dominated, as argued in Zhang et al. (2024).

3. A STRATIFIED DENSITY PROFILE

The slopes of afterglows produced by forward shocks depend on the density profile of the circum-burst medium. The density profile of the circum-burst medium is usually described by $n(R) \propto R^{-k}$, where $k = 0$ corresponds to a homogeneous medium, while $k = 2$ corresponds to a stellar wind from the GRB progenitor (Dai & Lu 1998; Chevalier & Li 2000; Panaitescu & Kumar 2000). In the wind case, for a constant mass loss rate \dot{M} and wind velocity v_w , one has $n = Ar^{-2}$, where $A = 3 \times 10^{35} A_* \text{cm}^{-1}$, scaled to $A_* = (\dot{M}/10^{-5} M_{\odot} \text{yr}^{-1})(v_w/10^3 \text{Kms}^{-1})^{-1}$.

The TeV light curve of GRB 221009A rises with a slope of $\alpha = 1.82_{-0.18}^{+0.21}$ before the peak (LHAASO Collaboration 2023). This rising phase is interpreted as the onset of the TeV afterglow, where the ejecta is coasting before deceleration. During the coasting phase, the bulk Lorentz factor of the afterglow shock is roughly a constant. The flux resulted from the synchrotron self-Compton process (SSC) rises with a slope as $\alpha = \frac{8-(p+2)k}{4}$ if the observed frequency lies above the peak frequency of the SSC spectrum (LHAASO Collaboration 2023). The rising slope $\alpha = 1.82_{-0.18}^{+0.21}$ of the TeV light curve is consistent with the constant-density medium (i.e., $k = 0$). Note that this conclusion applies only to the small radius where the early ($t < 18$ s) TeV emission is produced.

The density at a larger distance could be different and can only be constrained by late-time multi-wavelength data. Fermi-LAT measurement of GeV emission at $T_0 + 20000$ s suggests a low density at large radii, as we show below. The High Energy Stereoscopic System (H.E.S.S.) began observations 2.5 days after the trigger, yielding an upper limit on the TeV flux (Aharonian et al. 2023). This upper limit implies a small TeV to keV flux ratio at 2.5 days, which also supports a low density at larger radii.

3.1. Lower Limit on the Density at Small Radii

We assume that the TeV emissions observed by LHAASO are produced by the afterglow synchrotron self-Compton (SSC) process. Then we can use the TeV flux to constrain the density of the surrounding medium. The SSC flux without considering the Klein-Nishina (KN) effect can be expressed as (Sari & Esin 2001).

$$F_\nu = \begin{cases} F_m^{\text{IC}} \left(\frac{\nu}{\nu_m^{\text{IC}}}\right)^{\frac{1}{3}}, & \nu < \nu_m^{\text{IC}} \\ F_m^{\text{IC}} \left(\frac{\nu}{\nu_m^{\text{IC}}}\right)^{-\frac{p-1}{2}}, & \nu_m^{\text{IC}} < \nu < \nu_c^{\text{IC}} \\ F_m^{\text{IC}} \left(\frac{\nu}{\nu_m^{\text{IC}}}\right)^{\frac{1}{2}} \left(\frac{\nu}{\nu_c^{\text{IC}}}\right)^{-\frac{p}{2}}, & \nu > \nu_c^{\text{IC}} \end{cases} \quad (4)$$

where $F_m^{\text{IC}} = \tau_{\text{IC}} F_{\nu, \text{max}}$ is the peak flux density for SSC, which scales as $F_m^{\text{IC}} \propto n_0^{5/4}$ in a constant-density medium, p is the spectral index for shock-accelerated electrons ($dN_e/d\gamma'_e \propto \gamma'_e{}^{-p}$), ν_m^{IC} and ν_c^{IC} are the characteristic inverse Compton frequency for minimal Lorentz factor γ'_m and cooling Lorentz factor γ'_c , respectively (see the Appendix A.1 for more details).

We assume that only a fraction ξ_e of shock-heated electrons are accelerated into a power-law form. The minimum break frequency in the SSC spectra is

$$h\nu_m^{\text{IC}} = 1 \text{ GeV} E_{1, \text{iso}, 55}^{3/4} \epsilon_e^4 \epsilon_{e, -1.5}^{-4} \epsilon_{\text{B}, -4}^{1/2} n_{0, -0.5}^{-1/4} t_{1.5}^{-9/4}, \quad (5)$$

where n_0 is the number density of the circum-burst medium, ϵ_e is the energy equipartition factor for non-

thermal electrons, ϵ_{B} is the energy equipartition factors for the magnetic field (we use $p = 2.3$ to derive the coefficient in the equation). Hereafter, we adopt the convention that subscript numbers x indicate normalisation by 10^x in cgs units.

LHAASO observations show the spectral index in 0.2-7 TeV is $\beta \simeq -1.4$, suggesting $\nu_m^{\text{IC}} \lesssim 200 \text{ GeV}$. This imposes a limit on $k_e \equiv \epsilon_e/\xi_e$,

$$k_e \leq 0.15 E_{1, \text{iso}, 55}^{-3/16} \epsilon_{\text{B}, -4}^{-1/8} n_{0, -0.5}^{1/16}. \quad (6)$$

In the spectral region $\nu \geq \nu_m^{\text{IC}}$, the flux density at $h\nu = 300 \text{ GeV}$ at 30s is given by

$$F_\nu(300 \text{ GeV}) = 0.005 \mu\text{Jy} E_{1, \text{iso}, 55}^{\frac{7+3p}{8}} k_e^{2(p-1)} \xi_{e, 0}^{\frac{11-p}{8}} n_{0, -0.5}^{\frac{p+1}{4}} \epsilon_{\text{B}, -4}^{-4}. \quad (7)$$

Since the KN effect will only suppress the SSC process, the flux given by Equation (7) can be regarded as an upper limit for the observed flux density, which is $F_{\nu, \text{obs}}(300 \text{ GeV}) = 0.0052 \mu\text{Jy}$ at $T^* + 30$ s (LHAASO Collaboration 2023). Note that, if $\nu_c^{\text{IC}} < 300 \text{ GeV}$, the spectrum is steeper than $F_\nu \propto \nu^{(1-p)/2}$, then the inequality $F_\nu(300 \text{ GeV}) \geq F_{\nu, \text{obs}}(300 \text{ GeV})$ is still applicable.

Considering that the afterglow synchrotron flux should not be greater than the observed flux by Fermi/LAT at 100 MeV at $T^* + 110$ s, we obtain $\xi_{e, 0} k_e^{p-1} \leq E_{\text{iso}, 55}^{-\frac{(p+2)}{4}} \epsilon_{\text{B}, -4}^{-\frac{(p-2)}{4}}$ (LHAASO Collaboration 2023). Utilizing the above maximum value of $\xi_e k_e^{p-1}$ and k_e , we obtain a lower limit on the circum-burst density at the shock radius corresponding to $t = T^* + 30$ s,

$$n_0 \geq 0.1 \text{ cm}^{-3} E_{1, \text{iso}, 55}^{-\frac{9-p}{21-p}} \epsilon_{\text{B}, -4}^{-\frac{2(7-p)}{21-p}}. \quad (8)$$

Below we will show that the radio afterglow, GeV emission observed by Fermi/LAT and the H.E.S.S. TeV upper limit combine to constrain the circum-burst density to be lower than Equation (8) at larger radii.

3.2. Upper Limit on the Density at Large Radii

The observed flux at 1 GeV is $\mathcal{F}_{\text{obs}, \text{GeV}} \sim 2 \times 10^{-10} \text{ erg cm}^{-2} \text{ s}^{-1}$ at $T_0 + 20000$ s (Liu et al. 2023) and the flux at 1 keV at the same time is $\mathcal{F}_{\text{obs}, \text{keV}} \sim 10^{-9} \text{ erg cm}^{-2} \text{ s}^{-1}$. Considering that the GeV flux of the afterglow is contributed by both the SSC emission and synchrotron emission while the flux at 1 keV is fully contributed by the synchrotron emission, the flux ratio between the SSC component and the synchrotron component should be smaller than 0.2, i.e., $\mathcal{F}_{\text{GeV}}^{\text{IC}}/\mathcal{F}_{\text{keV}}^{\text{syn}} \leq 0.2$. Using this flux ratio, we can obtain an upper limit on the circum-burst density, in combination with the radio afterglow data.

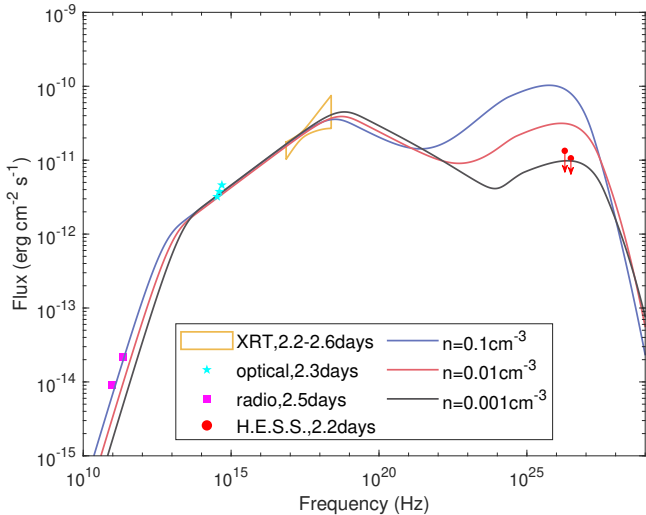


Figure 1. Spectra energy distribution of the afterglow emission at $T_0 + 2.5$ days. The red points denote the 95% C.L. upper limits from H.E.S.S. Collaborations. The blue, red and black lines represent the afterglow models with density $n_0 = 0.1\text{cm}^{-3}$, $n_0 = 0.01\text{cm}^{-3}$ and $n_0 = 0.001\text{cm}^{-3}$, respectively. The corresponding values of ϵ_B are 3×10^{-4} , 1×10^{-3} and 4×10^{-3} , respectively for three lines. Other parameters are $E_{\text{II,iso}} = 2.2 \times 10^{53}\text{erg}$, $p = 2.4$, $\epsilon_e = 0.1$, and $\xi_e = 0.1$.

The characteristic cooling break in the SSC spectrum are $h\nu_c^{\text{IC}} = 100\text{PeV}E_{\text{II,iso},54}^{-5/4}\epsilon_B^{-7/2}n_{0,-9/4}^{-1}t_{4.3}^{-1/4}$ while the KN peak $E_{\text{c,KN}}^{\text{IC}} = 0.26\text{TeV}E_{\text{II,iso},54}^{-1/4}\epsilon_B^{-1}n_{0,-3/4}^{-1}t_{4.3}^{-1/4}$ is around TeV. So the GeV band probably lies between ν_m^{IC} and ν_c^{IC} at $T_0 + 20000\text{s}$. The spectral index of X-ray emission measured by Swift XRT is $\beta = -0.78 \pm 0.011$ at $T_0 + 26000\text{s}$, consistent with the slow cooling phase. With the spectra regimes of $\nu_m < \nu_{\text{keV}} < \nu_c$ and $\nu_m^{\text{IC}} < \nu_{\text{GeV}} < \nu_c^{\text{IC}}$, the expected ratio between the SSC flux at 1 GeV and the synchrotron flux at 1 keV is

$$\frac{\mathcal{F}_{\text{GeV}}^{\text{IC}}}{\mathcal{F}_{\text{keV}}^{\text{syn}}} = 0.019E_{\text{II,iso},54}^{\frac{p+1}{8}}k_{e,-1.5}^{p-1}n_{0,-0.5}^{\frac{7-p}{8}}. \quad (9)$$

As $k_e \equiv \epsilon_e/\xi_e$, a large ϵ_e or small ξ_e will cause a high value of GeV-keV ratio. The value of k_e can be constrained by the spectral energy distribution at $T_0 + 2.5\text{d}$, as shown in Figure 1. The radio to X-ray afterglows are produced by the synchrotron emission of accelerated electrons. From Figure 1, we can see that the radio to X-ray emissions do not follow a single power law, indicating the presence of a spectral break between radio and X-ray frequencies. A plausible explanation is that the break ν_m lies at $\nu_m \geq 3 \times 10^{12}\text{Hz}$ (The possibility that the break is the self-absorption frequency ν_a is disfavored, see the Appendix B). The inequality arises from that the radio emission could include contributions from both forward shock emission and reverse shock emission.

As the break frequency ν_m is given by

$$\nu_m = 2.3\text{GHz}E_{\text{II,iso},54}^{1/2}k_{e,-1.5}^2\epsilon_{B,-4}^{1/2}t_{5.3}^{-3/2}, \quad (10)$$

we obtain

$$k_e \geq 1.1E_{\text{II,iso},54}^{-1/4}\epsilon_{B,-4}^{-1/4}. \quad (11)$$

With this lower limit of k_e , we then obtain an upper limit on the circum-burst density by using Equation (9),

$$n_0 \leq 0.007\text{cm}^{-3}E_{\text{II,iso},54}^{-\frac{3-p}{7-p}}\epsilon_{B,-4}^{\frac{2(p-1)}{7-p}}. \quad (12)$$

Such a low density is dramatically different from the constraint we derived from the early TeV afterglow $n_0 \geq 0.1\text{cm}^{-3}E_{\text{I,iso},55}^{-0.36}\epsilon_{B,-4}^{-0.5}$. It is hard to reconcile the discrepancy by increasing ϵ_B , because $h\nu_c \propto E_{\text{I,iso}}^{-1/2}\epsilon_B^{-3/2}n_0^{-1}$ is more sensitive to ϵ_B and the requirement $h\nu_c \geq 10\text{keV}$ at $T_0 + 4000\text{s}$ leads to

$$n_0 \leq 0.25\text{cm}^{-3}E_{\text{I,iso},55}^{-1/2}\epsilon_{B,-4}^{-3/2}. \quad (13)$$

The H.E.S.S. upper limit at 2.5 day also implies a low circum-burst density. In TeV band, the flux is suppressed by the KN effect and internal $\gamma\gamma$ absorption, so it can only be studied numerically. We model the SED of afterglows at 2.5 days in Figure 1 with the synchrotron plus SSC emission, and find that only when $n_0 < 0.01\text{cm}^{-3}$ the model can fit the data.

3.3. A Stratified Density Profile: Transition from a Constant-density Medium to a Wind Medium

Therefore, we consider a stratified density profile given by

$$n(r) = \begin{cases} n_0, & r < r_c \\ Ar^{-2}, & r \geq r_c \end{cases} \quad (14)$$

The transition radius from constant-density region to the wind region occurs at $r_c = \sqrt{A/n_0} = 5.5 \times 10^{17}\text{cm}A_{\star,-1}^{1/2}n_{0,-1}^{-1/2}$, corresponding to a transition time $t_c = 210E_{\text{I,iso},55}^{-1}A_{\star,-1}^2n_{0,-1}^{-1}\text{s}$. We assume the transition time is later than the jet break time $T^* + 670\text{s}$, so the wind parameter should satisfy

$$A_{\star} \geq 0.17E_{\text{I,iso},55}^{1/2}n_{0,-1}^{1/2}. \quad (15)$$

The standard wind-like profile ($k = 2$) is based on the assumption of a constant mass loss rate \dot{M} and wind velocity v_w . However, the dynamics of the stellar wind right before the death of the massive star is highly uncertain. Strong deviations from a density slope of $k = 2$ may be expected in the region very close to the GRB progenitor, due to the short evolutionary timescales after core helium exhaustion and the effects of near-critical rotation, which can significantly alter wind

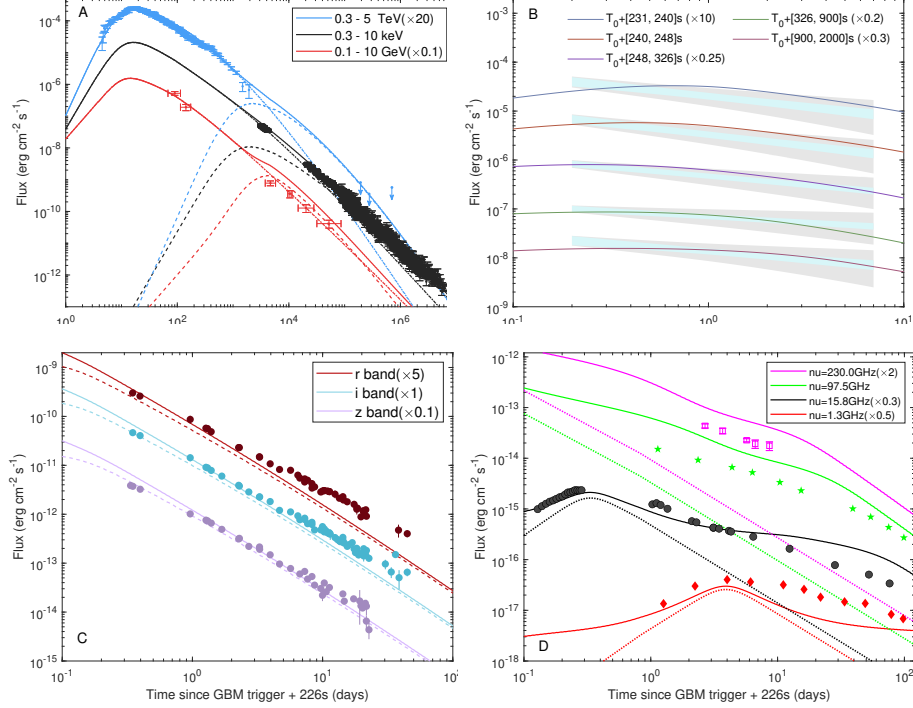


Figure 2. Modeling of the multi-wavelength data of GRB 221009A with the standard afterglow theory. Panel A displays the light curves in the energy band of TeV (0.3-5 TeV), keV (0.3-10 keV) and GeV (0.1-10 GeV). The upper limits after 10^5 s show the H.E.S.S. data in the energy range 0.65-10 TeV. The solid lines represent the sum of forward shock emission from the narrow core (dot-dashed lines) and the wide wing (dashed lines). Panel B displays the spectra between 0.2-7 TeV measured by LHAASO in different time intervals (LHAASO Collaboration 2023). The light blue band and grey band denote the systematic uncertainties and EBL-related uncertainties, respectively. The solid line represents the sum of forward shock SSC emission of the narrow core and wide wing. Panel C displays the optical light curves in r band (red), i band (blue) and z band (purple). All optical data points are corrected only by the galactic extinction (Schlafly & Finkbeiner 2011). The solid lines represent the sum of forward shock emission from the narrow core and the wide wing (dashed lines). For brevity, the lines for the emission from the narrow core are not shown. Panel D shows the radio light curves at 230GHz (pink square), 97.5GHz (green star), 15.8GHz (black circle) and 1.5GHz (red diamond). The solid lines represent the sum of forward shock emission from the narrow core, the forward shock emission from the wide wing, and the reverse shock emission of the wide wing. The dotted line represents the reverse shock emission of the wide wing.

properties. For example, if $\dot{M} \propto t^a$ and $v_w \propto t^b$, we have $\rho \propto r^{-2+(a-b)/(1+b)}$. A special mass loss rate and wind velocity ($a = 3b + 2$) during the last few hundred years of the star's life can lead to $k = 0$ in the region close to the GRB progenitor (Yoon et al. 2006; De Colle et al. 2012). In addition, if the GRB occurs in massive stellar clusters, the circum-burst medium is much more complicated due to the colliding wind effect (Mimica & Giannios 2011). In this case, one would expect an enhanced density due to the shocked colliding winds and a freely expanding wind at a larger distance.

4. MODEL FITS OF THE MULTI-WAVELENGTH AFTERGLOW DATA

We consider an on-axis two-component jet model with the angular distribution described in Equation (1) expanding into a stratified circum-burst medium (Equation (14)). The model uses shock dynamics given in the Appendix A.2. We assume that a fraction ξ_e of shock-

heated electrons are accelerated into a power law distribution with a spectral index of p : $dN_e/d\gamma'_e \propto \gamma'_e{}^{-p}$, where γ'_e is the electron Lorentz factor. The complete KN cross section for the inverse Compton scattering has been considered and the internal $\gamma\gamma$ absorption within the emitting region has been taken into account (see the Appendix A.2).

For the narrow core, we use the isotropic energy $E_{I,\text{iso}} = 4\pi\epsilon_{\text{I}}$ to solve the shock dynamics. For the wing component, since the energy has an angular distribution, it is reasonable to use the average isotropic energy in the solid angle between θ_j and θ in the calculation, which is given by

$$\bar{E}_{\text{II},\text{iso}}(\theta) = \frac{4\pi \int_{\theta_j}^{\theta} \epsilon_{\text{II}} f(\theta') \sin \theta' d\theta'}{\int_{\theta_j}^{\theta} \sin \theta' d\theta'}. \quad (16)$$

$\bar{E}_{\text{II},\text{iso}}(\theta)$ starts to increase from θ_j and decreases as a power-law $\bar{E}_{\text{II},\text{iso}} \propto \theta^{-a}$ when $\theta \gg \theta_j$.

4.1. The Optical to TeV Afterglows

The parameters of the angular profile of the wide wing can be estimated from the X-ray afterglow light curve analytically. For a wing with angular profile $dE/d\Omega \propto \theta^{-a}$, the light curve of the synchrotron emission from the forward shock is given by (Beniamini et al. 2022; Zhang et al. 2024)

$$F_\nu \propto \begin{cases} t^{-\frac{a}{3(4-a)}}, & \nu < \nu_m \\ t^{-\frac{2(3p-1)-a(p-1)}{2(4-a)}}, & \nu_m < \nu < \nu_c \\ t^{-\frac{2(3p-2)-a(p-2)}{2(4-a)}}. & \nu > \nu_c \end{cases} \quad (17)$$

Before 0.8 d, the power-law slope of the X-ray afterglow is $\alpha = -1.52$, suggesting an angular profile index of $a = 0.2$. After 0.8 d, the slope becomes steeper with $\alpha = -1.66$, leading to $a = 0.7$.

The bulk Lorentz factor is $\Gamma = 23E_{\text{II,iso},54}^{1/4}A_{\star,-1}^{-1/4}$ at 0.8 d, suggesting that the transition angle from a shallow angular profile to a steeper angular profile is $\theta_{c,w} \sim \Gamma^{-1} \approx 2.5^\circ E_{\text{II,iso},54}^{-1/4}A_{\star,-1}^{1/4}$.

We model the multi-wavelength afterglow data of GRB 221009A with the two-component jet model, which is shown in Figure 2. We first assume that there is no lateral expansion for both jet components. We find that this model can explain the TeV, X-ray and optical afterglows, with the model parameter values given in Table 1.

The early TeV afterglow emission originates from the SSC emission of the narrow jet component. At times later than 10^4 s, the SSC emission from the wing component becomes dominant, and its flux is consistent with the upper limits imposed by H.E.S.S. observations. The X-ray afterglow at times later than 10^4 s is produced by the wing component through the synchrotron emission. The optical afterglow is also produced by the synchrotron emission of the wing component. The model flux is insufficient to explain the optical data after tens of days, which could be attributed to extra contribution from a supernova (Fulton et al. 2023; Levan et al. 2023; Srinivasaragavan et al. 2023; Blanchard et al. 2023).

The isotropic energy of the narrow core is $4\pi\epsilon_{\text{I}} = 9 \times 10^{54}$ erg, while the isotropic energy of the wing at $\theta = \theta_{c,w}$ is $4\pi\epsilon_{\text{II}}/\sqrt{2} = 2.8 \times 10^{53}$ erg. The indices of the angular profile of the wing, $a_1 = 0$ and $a_2 = 0.8$, are consistent with the above analytical estimate. The acceleration fraction $\xi_e = 0.15$ for the wide wing is an order of magnitude higher than that in O'Connor et al. (2023) and Gill & Granot (2023), which avoids to overproduce the TeV flux measured by H.E.S.S. at 2.5 days.

The theoretical flux at GeV band slightly exceeds the observational data at $\sim 10^4$ s, during which both the narrow jet and wide wing contribute to the flux. Semi-

analytical models and numerical simulations have shown that lateral expansion may be important for narrow jets (Granot & Piran 2012; Lu et al. 2020), so our calculation may overestimate the emission flux from the narrow core component after its jet break time if the later expansion occurs in structured jets (Gottlieb et al. 2021). The model considering the lateral expansion for the narrow core is shown in Figure 3, which now agrees better with the GeV data.

4.2. The Radio Afterglow

The radio afterglow of GRB 221009A may be produced by both the forward shock emission and reverse shock emission. Since the narrow jet is likely to be Poynting-flux-dominated, we do not consider the reverse shock emission from this component. The reverse shock emission in our model comes from the wide wing.

The early radio data around 0.2 d exhibit a spectral shape $F_\nu \propto \nu^{5/2}$, indicating that the observed frequency (~ 15 GHz) is between the self-absorption frequency and the minimum frequency, i.e., $\nu_m < \nu < \nu_a$. This feature is inconsistent with the forward shock emission, which has a much higher ν_m . Therefore, the early radio is probably dominated by the reverse shock.

Since the deceleration time of the wide jet is ~ 3000 s, the wide jet can be regarded as a thin shell. After the deceleration, the Lorentz factor of reverse shock follows the relation $\Gamma_3 \propto R^{-g}$. For the wind environment, we take $g = 1$, and the rising slope of reverse shock emission in the spectral regime of $\nu_{m,rs} < \nu < \nu_{a,rs}$ is $\alpha = \frac{5(8+5g)}{14(1+2g)} = 1.55$ (Zou et al. 2005), which is close to the observed rising slope $\alpha = 1.4$ (Bright et al. 2023).

However, the observed decay slope of the radio afterglow, $\alpha = -0.8$, is much shallower than the prediction by the reverse shock in a top-hat jet, which is $\alpha \approx -2$. Zhang et al. (2024) studied the reverse shock evolution in a structured jet and found the decay slope can be shallower when the initial Lorentz factor of the jet has an angular structure, i.e., $\Gamma_0 \propto \theta^{-k_r}$ (see Appendix C). Considering this effect, the decaying slope of the reverse shock emission is $\alpha = -1.35$ for $a = 0$ and $\alpha = -1.54$ for $a = 0.8$, as discussed in Appendix C.

From Figure 2 and 3, we can see that the model does not explain the radio afterglow data satisfactorily. The forward shock emission exceeds the high-frequency radio data by a factor of about 2 in the case assuming no lateral expansion for the narrow jet and by a factor of 1.5 assuming lateral expansion.

Indeed, it is found that the light curves of radio afterglows of many GRBs can not be explained satisfactorily by the standard afterglow theory (e.g. Levine et al. 2023). This could indicate our lack of knowledge

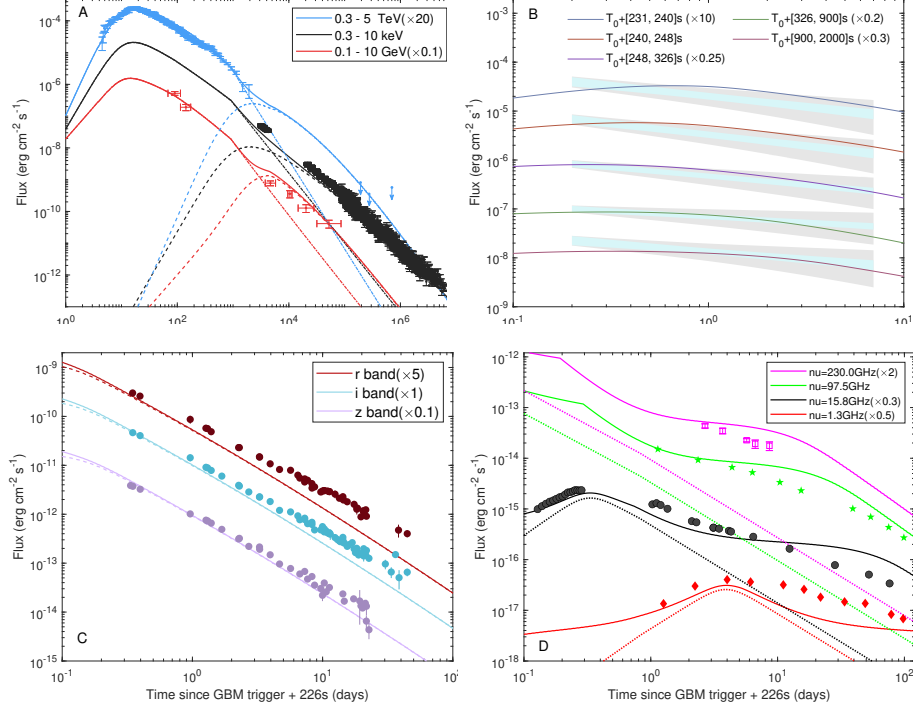


Figure 3. Same as Figure 2, but assuming that the narrow core has lateral expansion when the bulk Lorentz factor drops to $\Gamma_1 \leq \theta_j^{-1}$.

about the radio afterglow. Below we discuss some non-standard scenarios that could possibly resolve the discrepancy in the radio afterglows of GRB 221009A.

5. NON-STANDARD AFTERGLOW MODEL

In the standard model of afterglows, the microphysical parameters ϵ_e , ϵ_B , ξ_e and p are usually assumed to be a constant in the whole afterglow. The assumption simplifies the modeling and can explain afterglows of many GRBs. However, for those GRBs which are thoroughly investigated (e.g. GRB 130427A & GRB 170817A), time-evolving microphysics parameters are proposed to explain some unusual behaviour of afterglows (e.g. Maselli et al. 2014; Takahashi et al. 2022).

For GRB 221009A, the radio observations after 10 days impose a stringent limit on ν_m and k_e . At $T_0 + 54$ days, the spectrum between X-ray and radio is not a single power-law, so ν_m is required to be higher than 3×10^{11} Hz, which gives

$$k_e \geq 1.7 E_{\text{II,iso},54}^{-1/4} \epsilon_{B,-3}^{-1/4}. \quad (18)$$

On the other hand, we obtain an upper limit of $k_e \lesssim 0.4$ at 2.5 d from the SED modeling for $A_* = 0.17$ and $E_{\text{II,iso}} = 10^{54}$ erg. The discrepancy of k_e at the two times can not be solved by increasing ϵ_B in Equation (18), because the X-ray spectra at $T_0 + 26000$ s requires $h\nu_c \geq 10$ keV, resulting in $\epsilon_B \leq 1.2 \times 10^{-3} E_{\text{II,iso},54}^{1/4} A_{*, -1}^{-4/3}$. Furthermore, the isotropic equivalent energy decreases

with the time as $E_{\text{II,iso}} \propto t^{-\frac{\alpha}{4-\alpha}}$ for a structured jet (see the Appendix C), then a higher value of k_e is needed at 54 days. Thus, we speculate that k_e may increase with time in GRB 221009A. As $k_e = \epsilon_e / \xi_e$, the increase of k_e can be due to a decrease of ξ_e or an increase of ϵ_e .

5.1. Decreasing Acceleration Fraction ξ_e

The fraction of particles being accelerated in afterglow shocks depends on the conditions of the shock, including the bulk Lorentz factor, the magnetization parameter and the direction of the magnetic field (Sironi et al. 2015). Particle in cell (PIC) simulations find that the fraction of non-thermal electrons is about $\xi_e \sim 1 - 10\%$ (Spitkovsky 2008; Sironi et al. 2013). These simulations are conducted with the bulk Lorentz factor $\Gamma = 10 - 20$, which is different from the condition at early time when $\Gamma_0 > 100$. On the other hand, the magnetization degree can influence the direction of the magnetic field, possibly changing the acceleration fraction as well (Sironi et al. 2013). Thus the acceleration fraction ξ_e could be time-varying.

The high-frequency radio data ($\nu > 90$ GHz) lies above the power-law extrapolation of $F_\nu \propto \nu^{-0.2}$ from 1-20 GHz (see Figure 5 in Laskar et al. (2023)), implying that the forward shock may contribute to these bands. A decreasing ξ_e is helpful to avoid the overshoot in the radio flux at late times, because the synchrotron emission from the forward shock, $F_\nu \propto \epsilon_e^{-2/3} \xi_e^{5/3}$, is sensitive to ξ_e in

the spectral regime of $\nu < \nu_m$. For the X-ray and optical band, the evolution of ξ_e affects the light curve only slightly, as $F_\nu \propto \epsilon_e^{p-1} \xi_e^{2-p}$.

We assume the fraction of accelerated electrons decrease with time as $\xi_e \propto t^{-\alpha_\xi}$. In wind environment, the light curve of the structured jet is

$$F_\nu \propto \begin{cases} t^{-\frac{a}{3(4-a)} - \frac{5}{3}\alpha_\xi}, & \nu < \nu_m \\ t^{-\frac{2(3p-1)-a(p-1)}{2(4-a)} + \alpha_\xi(p-2)}, & \nu_m < \nu < \nu_c \\ t^{-\frac{2(3p-2)-a(p-2)}{2(4-a)} + \alpha_\xi(p-2)}. & \nu > \nu_c \end{cases} \quad (19)$$

The spectral index of X-ray afterglow measured by Swift XRT at later epochs is $\beta \approx -0.78$, suggesting a power-law index of $p \simeq 2.5$. After 0.8 d, the decay slopes of X-ray and high-frequency radio afterglows are $\alpha = -1.66$ and $\alpha = -0.78$ respectively. To fit the multi-wavelength data simultaneously, we need $a = 0.9$ and $\alpha_\xi = 0.4$. Because the bulk Lorentz factor of the afterglow shock decreases with time as $\Gamma \propto t^{-1/(4-a)}$, we then derive $\xi_e \propto \Gamma^{-1.24}$. Before 0.8 d, the decay slope of the X-ray afterglow is $\alpha = -1.52$, suggesting an angular profile index of $a = 0.2$. We assume $\xi_e = 1$ when the Lorentz factor is greater than 60.

We model the multi-wavelength afterglows with a time-varying ξ_e , which is shown in Figure 4. The fitting of radio data is improved. For low-frequency radio afterglows, the model flux is still below the data at later times. The excess could arise from some extra low-velocity ejecta components in this GRB, which may produce main radio emissions.

Since ϵ_e and ξ_e are coupled in the afterglow modeling, an alternative model is that ϵ_e is increasing with time. The main difference lies in that the X-ray and optical flux depends on ϵ_e as $F_\nu \propto \epsilon_e^{p-1}$. To fit the X-ray and optical light curves, we would need a steeper angular profile for the jet structure with $a \approx 2$.

5.2. Decaying Magnetic Field

In the standard afterglow shock model, we assume a homogeneous magnetic field in the downstream of the shock. Nonetheless, the realistic magnetic field may have a spatial distribution behind the shock. PIC simulations and theoretical analyses of relativistic collisionless shocks both suggest that the coherent length of magnetic fields is much smaller than the shock size of GRB afterglows (Chang et al. 2008; Lemoine 2015; Sironi et al. 2015).

Since the cooling time of radio-emitting electrons is much longer than the shock dynamic time, these electrons may radiate most of their energy at the back of the blast wave, where the magnetic field has decayed to a low value (Lemoine 2013; Wang et al. 2013). The

standard model assuming a constant ϵ_B may overestimate the radio flux at later epochs. Taking a realistic magnetic field might reduce the radio flux and solve the discrepancy.

6. CONCLUSIONS AND DISCUSSIONS

GRB 221009A, as the BOAT event, provides rich multi-wavelength afterglow data spanning from GHz to TeV energies. We find that the late-time multi-wavelength observations, including radio, X-ray, GeV and TeV, combine to constrain the density of the circum-burst medium to be lower than $n_0 < 0.01 \text{cm}^{-3}$, while the LHAASO observation at early time requires a constant-density medium with $n_0 \geq 0.1 \text{cm}^{-3} E_{1,\text{iso},55}^{-\frac{9-p}{21-p}} \epsilon_{B,-4}^{-\frac{2(7-p)}{21-p}}$ at small radii. Therefore, we propose a stratified density profile that incorporates a constant-density medium at small radii and a wind-like medium at large radii to explain the afterglows of GRB 221009A.

Motivated by the multi-wavelength data, we employ a two-component jet model, comprising a uniform narrow jet core and a structured wing. This model can explain the afterglows from optical to TeV bands, although the flux at high-frequency radio bands exceeds the data by a factor of two after the second day (see Figure 2 and 3). We find that the discrepancy could be resolved by invoking time-varying micro-physical parameters of afterglow shocks (see Figure 4).

The model flux is lower than the observed flux at low-frequency radio bands (e.g., $\nu = 1.3 \text{GHz}$) after ~ 2 days (see Figure 4). The excess could be due to some extra electron component, possibly resulting from low-velocity ejecta components or related to other acceleration mechanisms. The hard spectra of low-frequency radio data $\beta \approx -0.2$ is unusual in GRB afterglows, suggesting a hard injection spectra $p = 1.4$ for electrons, which is in contradiction to standard diffusive shock acceleration theory. Such a hard spectrum could result from some other acceleration mechanism, such as shear acceleration (Liu et al. 2017; Rieger & Duffy 2022).

Compared to previous single structured jet models (O'Connor et al. 2023; Gill & Granot 2023), our two-component structured jet model explains TeV and lower-energy afterglows simultaneously. Previous single structured jet models did not take into account the SSC process because the TeV data were not available. We calculate the SSC emission and include the TeV data in the modeling, providing a more self-consistent explanation for the multi-wavelength afterglows.

In our model, the beaming-corrected kinetic energy in the narrow core is $E_{1,b} = E_{1,\text{iso}}(1 - \cos \theta_j) = 5 \times 10^{50} \text{erg}$ (LHAASO Collaboration 2023). The kinetic energy in

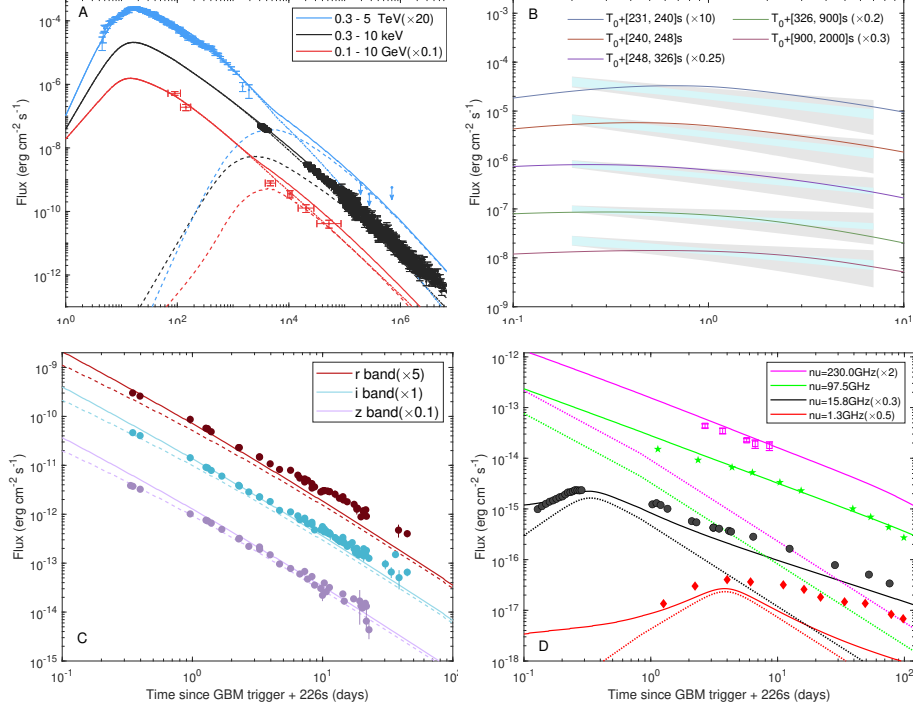


Figure 4. Same as Figure 2, but assuming that the acceleration fraction ξ_e in two components are decreasing with time.

Table 1. Parameter values used in the modeling of the multi-wavelength afterglow data. The subscript I and II represent the parameters for the narrow core and wide wing, respectively. Forward shock1 (FS1) denotes the standard forward shock model shown in Figure 2, while Forward shock2 (FS2) denotes the non-standard forward shock model with a time-varying $\xi_e \propto \Gamma^{-\alpha_\Gamma}$, which was shown in Figure 4. We use $\alpha_{I,\Gamma} = 1.35$ and $\alpha_{II,\Gamma} = 1.25$ in the non-standard case. The parameter values for the density profile are $n_0 = 0.2 \text{ cm}^{-3}$ and $A_* = 0.17$.

	$4\pi\epsilon_I(\text{erg})$	θ_j	$\Gamma_{I,0}$	$\epsilon_{I,e}$	$\epsilon_{I,B,-3}$	$\xi_{I,e}$	p_I	$4\pi\epsilon_{II}(\text{erg})$	$\theta_{c,w}$	$\Gamma_{II,0}$	a_1	a_2	$\epsilon_{II,e}$	$\epsilon_{II,B,-3}$	$\xi_{II,e}$	p_{II}
FS1	9×10^{54}	0.6°	560	0.04	1	1	2.2	4×10^{53}	3°	60	0	0.8	0.06	2	0.15	2.4
FS2	9×10^{54}	0.6°	560	0.04	1	—	2.2	4×10^{53}	3°	60	0	1.0	0.06	2	—	2.5
RS	—	—	—	—	—	—	—	4×10^{53}	3°	60	0	0.8/1.0 ^a	0.04	0.5	0.01	2.2

^a This parameter follows the forward shock.

the structured wing is $E_{II,b} = 2 \int_{\theta_j}^{\Theta} \frac{dE}{d\Omega} d\Omega$, where θ is the angle corresponding to the last observing time t before seeing the maximum angle Θ . The beaming-corrected energy increase as $E_{II,b} \propto \theta^2 \propto t^{\frac{2-\alpha}{4-\alpha}}$ (Beniamini et al. 2022). We find the beaming-corrected energy of the structured wing is $E_{II,b} = 5.7 \times 10^{51} (t/100\text{days})^{3/8} \text{erg}$ for $a_2 = 0.8$ and $E_{II,b} = 4.9 \times 10^{51} (t/100\text{days})^{1/3} \text{erg}$ for $a_2 = 1$. These values are significantly lower than the energy budget required by single structured jet models, which are $8 \times 10^{52} (t/80\text{days})^{0.372} \text{erg}$ in the model of

O'Connor et al. (2023) and $4 \times 10^{52} (t/100\text{days})^{0.375} \text{erg}$ in the model of Gill & Granot (2023), respectively.

The authors thank Katsuaki Asano, Hai-Ming Zhang, Liang-Duan Liu and Yu-Jia Wei for useful discussions. This work is supported by the National Natural Science Foundation of China (grant numbers 12333006, 12121003, U2031105).

A. METHODS

A.1. Analytical Methods

The analytical solution of the bulk Lorentz factor Γ and the radius R of relativistic blast wave in an arbitrary power-law density profile $n = Ar^{-k}$ are give by (Granot & Sari 2002)

$$\Gamma = 1.15^{2-k} \left(\frac{(17-4k) E_{\text{iso}}}{4^{5-k} (4-k)^{3-k} \pi A m_{\text{p}} c^{5-k} t_z^{3-k}} \right)^{\frac{1}{2(4-k)}}, \quad R = 1.3^{-k-1} \left(\frac{(17-4k)(4-k) E_{\text{iso}} t_z}{4\pi A m_{\text{p}} c} \right)^{\frac{1}{4-k}}, \quad (\text{A1})$$

where $t_z = t/(1+z)$ is the time corrected by redshift, 1.15 and 1.3 are numerical correction factors. Assuming the injection spectra of electrons is a single power law $dN_e/d\gamma'_e \propto \gamma_e'^{-p}$. The prime marks the comoving frame of the shock. The minimum Lorentz factor and the cooling Lorentz factor are

$$\gamma'_m = \frac{\epsilon_e p - 2 m_{\text{p}}}{\xi_e p - 1 m_e} (\Gamma - 1), \quad \gamma'_c = \frac{6\pi m_e c}{\sigma_{\text{T}} \Gamma B'^2 t_z}, \quad (\text{A2})$$

where ϵ_e is the equipartition factor of electrons, and ξ_e is the fraction of accelerated electrons. The magnetic field in the comoving frame is $B' = \sqrt{8\pi \epsilon_{\text{B}} n m_{\text{p}} c^2 (\Gamma - 1)(\hat{\gamma}\Gamma + 1)/(\hat{\gamma} - 1)}$, where $\hat{\gamma}$ is the adiabatic index of the shock. We use the fitting formula for $\hat{\gamma}$ from Pe'er (2012), which is $(5 - 1.21937z + 0.18203z^2 - 0.96583z^3 + 2.32513z^4 - 2.39332z^5 + 1.07136z^6)/3$, where $z = \zeta/(0.24 + \zeta)$, $\zeta = (\frac{\Gamma\beta_{\text{sh}}}{3})(\frac{\Gamma\beta_{\text{sh}} + 1.07(\Gamma\beta_{\text{sh}})^2}{1 + \Gamma\beta_{\text{sh}} + 1.07(\Gamma\beta_{\text{sh}})^2})$, and $\beta_{\text{sh}} = \sqrt{1 - \Gamma^{-2}}$ is the velocity of the shock.

In a constant medium ($k = 0$), the characteristic break frequencies in the synchrotron emission spectrum are

$$\nu_{\text{m}} = \frac{\Gamma \gamma'_m{}^2 \nu'_L}{1+z} = 2.4 \times 10^{11} \text{Hz} E_{\text{iso},55}^{1/2} k_{e,-1}^2 \epsilon_{\text{B},-4}^{1/2} t_5^{-3/2}, \quad \nu_{\text{c}} = \frac{\Gamma \gamma'_c{}^2 \nu'_L}{1+z} = 6.7 \times 10^{17} \text{Hz} E_{\text{iso},55}^{-1/2} n_{0,-0.5}^{-1} \epsilon_{\text{B},-4}^{-3/2} t_5^{-1/2}, \quad (\text{A3})$$

where $\nu'_L = eB'/2\pi m_e c$ is the Lamour frequency of electrons. The characteristic break energies for SSC emission are

$$h\nu_{\text{m}}^{\text{IC}} = 2\gamma'_m{}^2 h\nu_{\text{m}} = 65 \text{GeV} E_{\text{iso},55}^{3/4} k_{e,-1}^4 \epsilon_{\text{B},-4}^{1/2} n_{0,-0.5}^{-1/4} t_{1.5}^{-9/4}, \quad h\nu_{\text{c}}^{\text{IC}} = 2\gamma'_c{}^2 h\nu_{\text{c}} = 28 \text{PeV} E_{\text{iso},55}^{-5/4} \epsilon_{\text{B},-4}^{-7/2} n_{0,-0.5}^{-9/4} t_{1.5}^{-1/4}. \quad (\text{A4})$$

If $h\nu_{\text{c}}^{\text{IC}} \gtrsim \Gamma \gamma'_c m_e c^2$, the cooling break energy of SSC flux is $E_{\text{c,KN}}^{\text{IC}} = 0.2 \Gamma \gamma'_c m_e c^2 = 0.75 \text{TeV} E_{\text{iso},55}^{-1/4} \epsilon_{\text{B},-4}^{-1} n_{0,-0.5}^{-3/4} t_{1.5}^{-1/4}$ due to the KN effect (Nakar et al. 2009).

In the observer frame, the peak flux density of the synchrotron and SSC emission are

$$F_{\nu,\text{max}} = (1+z) \frac{N_e P_{\nu}}{4\pi D_{\text{L}}^2} = 7 \text{Jy} E_{\text{iso},55} \xi_{e,0} \epsilon_{\text{B},-4}^{1/2} n_{0,-0.5}^{1/2}, \quad F_{\text{m}}^{\text{IC}} = \tau_{\text{IC}} F_{\nu,\text{max}} = 0.19 \mu\text{Jy} E_{\text{iso},55}^{5/4} \xi_{e,0} \epsilon_{\text{B},-4}^{1/2} n_{0,-0.5}^{5/4} t_{1.5}^{1/4}, \quad (\text{A5})$$

where $P_{\nu} = \sqrt{3} e^3 \Gamma B' / m_e c^2$ is the spectral power of synchrotron, $N_e = \int 4\pi r^2 \xi_e n(r) dr$ is the number of accelerated electrons, $D_{\text{L}} = 716 \text{Mpc}$ is the luminosity distance, $\tau_{\text{IC}} = n_0 \sigma_{\text{T}} R / 3$ is the optical depth of Inverse Compton.

A.2. Numerical Methods

The dynamical equations of the blast wave is described by (Huang et al. 1999)

$$\frac{d\Gamma}{dm_{\text{sw}}} = -\frac{\Gamma^2 - 1}{M_0 + [f + 2\Gamma(1-f)] m_{\text{sw}}}, \quad \frac{dR}{dt} = \frac{\beta_{\text{sh}} c}{1 - \beta_{\text{sh}}}, \quad (\text{A6})$$

where $M_0 = E_{\text{iso}}/(\Gamma_0 - 1)c^2$ is the initial mass of the ejecta, $m_{\text{sw}} = \int 4\pi r^2 \rho(r) dr$ is the swept-up mass and f is the radiative efficiency. We employ a constant isotropic energy $E_{\text{iso}} = 4\pi \epsilon_{\text{I}}$ for the narrow jet and the average isotropic energy $E_{\text{iso}} = \bar{E}_{\text{II,iso}}(\theta)$ for the wide jet.

We adopt $f = \epsilon_e (t'_{\text{syn}}{}^{-1}(\gamma'_m) + t'_{\text{IC}}{}^{-1}(\gamma'_m)) / (t'_{\text{syn}}{}^{-1}(\gamma'_m) + t'_{\text{IC}}{}^{-1}(\gamma'_m) + t'_{\text{ad}}{}^{-1})$ in our calculations, where $t'_{\text{ad}} = R/\Gamma\beta_{\text{sh}}c$ is timescale of adiabatic cooling, and $t'_{\text{syn}}(\gamma'_m)$ and $t'_{\text{IC}}(\gamma'_m)$ are cooling timescale of synchrotron and inverse Compton at γ'_m , respectively.

For electron spectra, we include the cooling of synchrotron and inverse Compton in the calculation $\gamma'_c = 6\pi m_e c / \sigma \Gamma B'^2 t_z (1 + f_{\text{KN}} Y)$, where $Y \equiv P_{\text{SSC}}/P_{\text{syn}}$ is the ratio between SSC power and synchrotron power. The

KN suppress factor is defined as $f_{\text{KN}} \equiv P_{\text{SSC}}^{\text{KN}}/P_{\text{SSC}}^{\text{T}}$, where the $P_{\text{SSC}}^{\text{T}} = \frac{4}{3}\pi\sigma_{\text{T}}c\gamma^2U'_{\text{syn}}$. The total energy loss rate of Compton scattering in KN regime is (Blumenthal & Gould 1970)

$$P_{\text{IC}}^{\text{KN}} = 12\gamma^2\sigma_{\text{T}}c \int_0^\infty \varepsilon' \frac{dn'}{d\varepsilon'} d\varepsilon' \int_0^1 \frac{qG(q, \Gamma_e)}{(1 + \Gamma_e q)^3} dq, \quad (\text{A7})$$

where $\Gamma_e = 4\gamma\varepsilon'/m_e c^2$, $G(q, \Gamma_e)$ is a function of KN cross section and $dn'/d\varepsilon'$ is the differential number density of synchrotron photons.

$$G(q, \Gamma_e) = 2q \ln q + (1 + 2q)(1 - q) + \frac{\Gamma_e^2 q^2 (1 - q)}{2(1 + \Gamma_e q)}. \quad (\text{A8})$$

The spectral power of synchrotron emission is

$$P'_\nu(\nu') = \frac{\sqrt{3}eB'}{m_e c^2} \int_{\gamma_m}^\infty \left(\frac{\nu'}{\nu'_c} \int_{\nu'/\nu'_c}^\infty K_{5/3}(z) dz \right) \frac{dN_e}{d\gamma'_e} d\gamma'_e, \quad (\text{A9})$$

where $\nu'_c = 3\nu'_L/2$ and $K_{5/3}(z)$ is the modified Bessel function. The spectra of SSC emission are calculated by the strict expressions from Blumenthal & Gould (1970).

$$\frac{dN'}{dE'} = \frac{3\sigma_{\text{T}}c}{4} \int_{\gamma_m}^\infty \left(\int \frac{dn'}{d\varepsilon'} \frac{d\varepsilon'}{\varepsilon'} \frac{G(q, \Gamma_e)}{\gamma_e^2} \right) \frac{dN_e}{d\gamma'_e} d\gamma'_e \quad (\text{A10})$$

where $q = w/\Gamma_e(1 - w)$, $w = E'/\gamma'_e m_e c$.

We also consider the internal $\gamma\gamma$ absorption for VHE photons in this code. The optical depth due to internal $\gamma\gamma$ absorption is

$$\tau_{\gamma\gamma, \text{int}}(\varepsilon'_\gamma, \varepsilon') = \int_{\varepsilon_{\text{th}}} \sigma_{\gamma\gamma}(\varepsilon'_\gamma, \varepsilon') \frac{R}{\Gamma} \frac{dn'}{d\varepsilon'} d\varepsilon' d\Omega, \quad (\text{A11})$$

where $\sigma_{\gamma\gamma}$ is the cross section, $\varepsilon_{\text{th}} = 2m_e^2 c^4 / \varepsilon'_\gamma (1 - \cos\theta)$ is the threshold energy of pair production. The cross section is

$$\sigma_{\gamma\gamma}(\varepsilon'_\gamma, \varepsilon') = \frac{3}{16} \sigma_{\text{T}} (1 - \beta_{\text{cm}}^2) \left[2\beta_{\text{cm}} (\beta_{\text{cm}}^2 - 2) + (3 - \beta_{\text{cm}}^4) \ln \left(\frac{1 + \beta_{\text{cm}}}{1 - \beta_{\text{cm}}} \right) \right], \quad (\text{A12})$$

where $\beta_{\text{cm}} = \sqrt{1 - 2m_e^2 c^4 / \varepsilon'_\gamma \varepsilon' (1 - \cos\theta)}$. For an intrinsic flux density F_ν , the flux density after the internal $\gamma\gamma$ absorption is $F_\nu \left(\frac{1 - e^{-\tau_{\gamma\gamma, \text{int}}}}{\tau_{\gamma\gamma, \text{int}}} \right)$.

For Figure 1, we use analytic methods from Equation (A1)&(A2) to compute dynamics and electron spectra, and then obtain the flux numerically with consideration of KN effects and internal absorptions.

B. ABSORPTION FREQUENCY AS THE BREAK FREQUENCY

In the main text we use ν_m as the break frequency between radio (97.5GHz) and X-ray (keV). Here we discuss the possibility that ν_a is the break frequency. The spectra of synchrotron emission are also affected by self-absorption. Frequency below absorption frequency ν_a drops rapidly as $F_\nu \propto \nu^{5/2}$. If the frequency break between X-ray and radio is attributed to self-absorption, ν_a is required to be $\nu_a \geq 400\text{GHz}$ at $T_0 + 10^5\text{s}$. The expression of ν_a depends on the values of ν_m and ν_c . We define ν_{a1} is the absorption frequency when ν_a is in the regime $\nu_a < \nu_m < \nu_c$. The values of ν_{a1} are

$$\nu_{a1} = \begin{cases} 5.3\text{GHz} E_{\text{iso}, 55}^{1/5} n_{0, -1}^{3/5} k_{e, -1}^{-1} \epsilon_{\text{B}, -4}^{1/5}, & k = 0 \\ 0.09\text{GHz} E_{\text{iso}, 55}^{-2/5} A_{\star, -1}^{6/5} k_{e, -1}^{-1} \epsilon_{\text{B}, -4}^{1/5} t_5^{-3/5}. & k = 2 \end{cases} \quad (\text{B13})$$

Apparently, ν_{a1} dissatisfy the condition $\nu_a \geq 400\text{GHz}$ unless we employ a very small value of k_e , which are $k_e \sim 10^{-3}$ in constant medium and $k_e \sim 10^{-5}$ in wind-like medium. However, such parameters are extremely small and fail to produce sufficient flux when the isotropic energy is 10^{55}erg . Although ν_{a1} is more sensitive to the density in wind profile $\nu_{a1} \propto A_{\star}^{6/5}$, large wind density $A_{\star} > 1$ enhances the TeV-keV ratio at later epochs, resulting overproduction in TeV band.

Moreover, applying such a small value of k_e would yield a very small ν_m . When ν_m is smaller than ν_a , expressions of ν_{a1} is not applicable. We define ν_{a2} as the absorption frequency when $\nu_m < \nu_a < \nu_c$. The absorption frequency ν_{a2} evolve as $\nu_{a2} \propto t^{-\frac{3p+2}{2(p+4)}}$ in constant medium and $\nu_{a2} \propto t^{-\frac{3(p+2)}{2(p+4)}}$ in wind-like medium. Since ν_{a2} is decreasing more rapidly with respect to time, we must have a larger ν_{a1} , which corresponds to more extreme parameters.

C. REVERSE SHOCK IN A STRUCTURED JET

In a structured jet, the angular energy distribution is $dE/d\Omega \propto \theta^{-a}$ and the initial Lorentz factor Γ_0 may have an angular distribution $\Gamma_0 \propto \theta^{-k_\Gamma}$ (Zhang et al. 2024). If the $k_\Gamma \leq 1$, the angular edges seen by observers are all decelerated since the radiative cone is $\theta \sim \Gamma^{-1}$. Hence, the forward shock dynamics is independent of the distribution of Γ_0 . In this case, emissions from the forward shock can be described by Equation (17). For the wind medium, the angular profile of the Lorentz factor of the shocked shell follows

$$\Gamma_3(\theta) = \Gamma_0(\theta) \left(\frac{R(\theta)}{R_{\text{dec}}(\theta)} \right)^{-g} \quad (\text{C14})$$

where $g = 1$ (Zou et al. 2005; Gao et al. 2013) for a reverse shock in the thin-shell approximation and R_{dec} is the deceleration radius of the ejecta, which scales as $R_{\text{dec}}(\theta) \propto E_{\text{II,iso}}(\theta)\Gamma_0(\theta)^{-2}$.

Our model used $k_\Gamma = 1$, so $\Gamma_3 \propto \theta^{-1}$. Using $R(\theta) = 2\Gamma_3(\theta)^2 t$, one obtains $\Gamma_3(\theta) \propto t^{-\frac{1}{4-a}}$, $\Gamma_0(\theta) \propto t^{-\frac{1}{4-a}}$, $E_{\text{II,iso}}(\theta) \propto t^{-\frac{a}{4-a}}$. The self-absorption frequency of reverse shock is $\nu_{\text{a,rs}} \propto E_{\text{II,iso}}^{\frac{6p-4}{7(p+4)}}(\theta)\Gamma_0^{-\frac{24p-16}{7(p+4)}}(\theta)t^{-\frac{13p+24}{7(p+4)}}(\nu_{\text{m,rs}} < \nu_{\text{a,rs}})$. We find $\nu_{\text{a,rs}} \propto t^{-1}$ when $k_\Gamma = 1$, which is closed to the observed scaling relation $\nu_{\text{a,rs}} \propto t^{-1.08 \pm 0.04}$ from Bright et al. (2023). Correspondingly, the minimum frequency is $\nu_{\text{m,rs}} \propto E_{\text{II,iso}}^{\frac{6}{7}}(\theta)\Gamma_0^{-\frac{24}{7}}(\theta)t^{-\frac{13}{7}} \propto t^{-1}$ and peak flux density is $F_{\nu,\text{max,rs}} \propto E_{\text{II,iso}}^{\frac{23}{21}}(\theta)\Gamma_0^{-\frac{23}{21}}(\theta)t^{-\frac{23}{21}} \propto t^{-\frac{3}{4-a}}$, respectively.

Thus the peak flux density of self-absorption $F_{\nu,\text{a}} = F_{\nu,\text{max}}(\frac{\nu_{\text{a,rs}}}{\nu_{\text{m,rs}}})^{\frac{1-p}{2}} \propto t^{-\frac{3}{4-a}}$ is consistent with the observed values $F_{\nu,\text{a}} \propto t^{-0.70 \pm 0.02}$ when the jet structure is flat with $a = 0$. After the crossing of absorption frequency, the reverse shock emission declines as $F_\nu = F_{\nu,\text{max}}(\frac{\nu}{\nu_{\text{m,rs}}})^{\frac{1-p}{2}} \propto t^{-\frac{3}{4-a} - \frac{p-1}{2}}$. Assuming $p = 2.2$, the slopes of decaying phase are $F_\nu \propto t^{-1.35}$ for $a = 0$ and $F_\nu \propto t^{-1.54}$ for $a = 0.8$.

REFERENCES

- Aharonian, F., Benkhali, F. A., Aschersleben, J., et al. 2023, *ApJL*, 946, L27, doi: [10.3847/2041-8213/acc405](https://doi.org/10.3847/2041-8213/acc405)
- An, Z.-H., Antier, S., Bi, X.-Z., et al. 2023, arXiv e-prints, arXiv:2303.01203, doi: [10.48550/arXiv.2303.01203](https://doi.org/10.48550/arXiv.2303.01203)
- Beniamini, P., Gill, R., & Granot, J. 2022, *MNRAS*, 515, 555, doi: [10.1093/mnras/stac1821](https://doi.org/10.1093/mnras/stac1821)
- Blanchard, P. K., Villar, V. A., Chornock, R., et al. 2023, arXiv e-prints, arXiv:2308.14197, doi: [10.48550/arXiv.2308.14197](https://doi.org/10.48550/arXiv.2308.14197)
- Blumenthal, G. R., & Gould, R. J. 1970, *Reviews of Modern Physics*, 42, 237, doi: [10.1103/RevModPhys.42.237](https://doi.org/10.1103/RevModPhys.42.237)
- Bright, J. S., Rhodes, L., Farah, W., et al. 2023, *Nature Astronomy*, 7, 986, doi: [10.1038/s41550-023-01997-9](https://doi.org/10.1038/s41550-023-01997-9)
- Burns, E., Svinikin, D., Fenimore, E., et al. 2023, *ApJL*, 946, L31, doi: [10.3847/2041-8213/acc39c](https://doi.org/10.3847/2041-8213/acc39c)
- Castro-Tirado, A. J., Sanchez-Ramirez, R., Hu, Y. D., et al. 2022, *GRB Coordinates Network*, 32686, 1
- Chang, P., Spitkovsky, A., & Arons, J. 2008, *ApJ*, 674, 378, doi: [10.1086/524764](https://doi.org/10.1086/524764)
- Chevalier, R. A., & Li, Z.-Y. 2000, *ApJ*, 536, 195, doi: [10.1086/308914](https://doi.org/10.1086/308914)
- Dai, C.-Y., Wang, X.-Y., Liu, R.-Y., & Zhang, B. 2023, *ApJL*, 957, L32, doi: [10.3847/2041-8213/ad0720](https://doi.org/10.3847/2041-8213/ad0720)
- Dai, Z. G., & Lu, T. 1998, *MNRAS*, 298, 87, doi: [10.1046/j.1365-8711.1998.01681.x](https://doi.org/10.1046/j.1365-8711.1998.01681.x)
- De Colle, F., Ramirez-Ruiz, E., Granot, J., & Lopez-Camara, D. 2012, *ApJ*, 751, 57, doi: [10.1088/0004-637X/751/1/57](https://doi.org/10.1088/0004-637X/751/1/57)
- Frail, D. A., Kulkarni, S. R., Sari, R., et al. 2001, *ApJL*, 562, L55, doi: [10.1086/338119](https://doi.org/10.1086/338119)
- Fulton, M. D., Smartt, S. J., Rhodes, L., et al. 2023, *ApJL*, 946, L22, doi: [10.3847/2041-8213/acc101](https://doi.org/10.3847/2041-8213/acc101)
- Gao, H., Lei, W.-H., Zou, Y.-C., Wu, X.-F., & Zhang, B. 2013, *NewAR*, 57, 141, doi: [10.1016/j.newar.2013.10.001](https://doi.org/10.1016/j.newar.2013.10.001)
- Gill, R., & Granot, J. 2023, *MNRAS*, 524, L78, doi: [10.1093/mnras/slad075](https://doi.org/10.1093/mnras/slad075)
- Gottlieb, O., Nakar, E., & Bromberg, O. 2021, *MNRAS*, 500, 3511, doi: [10.1093/mnras/staa3501](https://doi.org/10.1093/mnras/staa3501)
- Granot, J., & Kumar, P. 2003, *ApJ*, 591, 1086, doi: [10.1086/375489](https://doi.org/10.1086/375489)
- Granot, J., & Piran, T. 2012, *MNRAS*, 421, 570, doi: [10.1111/j.1365-2966.2011.20335.x](https://doi.org/10.1111/j.1365-2966.2011.20335.x)
- Granot, J., & Sari, R. 2002, *ApJ*, 568, 820, doi: [10.1086/338966](https://doi.org/10.1086/338966)
- Huang, Y. F., Dai, Z. G., & Lu, T. 1999, *MNRAS*, 309, 513, doi: [10.1046/j.1365-8711.1999.02887.x](https://doi.org/10.1046/j.1365-8711.1999.02887.x)
- Laskar, T., Alexander, K. D., Margutti, R., et al. 2023, *ApJL*, 946, L23, doi: [10.3847/2041-8213/acbfad](https://doi.org/10.3847/2041-8213/acbfad)

- Lemoine, M. 2013, *MNRAS*, 428, 845, doi: [10.1093/mnras/sts081](https://doi.org/10.1093/mnras/sts081)
- . 2015, *Journal of Plasma Physics*, 81, 455810101, doi: [10.1017/S0022377814000920](https://doi.org/10.1017/S0022377814000920)
- Lesage, S., Veres, P., Briggs, M. S., et al. 2023, *ApJL*, 952, L42, doi: [10.3847/2041-8213/ace5b4](https://doi.org/10.3847/2041-8213/ace5b4)
- Levan, A. J., Lamb, G. P., Schneider, B., et al. 2023, *ApJL*, 946, L28, doi: [10.3847/2041-8213/acc2c1](https://doi.org/10.3847/2041-8213/acc2c1)
- Levine, D., Dainotti, M., Fraija, N., et al. 2023, *MNRAS*, 519, 4670, doi: [10.1093/mnras/stac3730](https://doi.org/10.1093/mnras/stac3730)
- LHAASO Collaboration. 2023, *Science*, 380, 1390, doi: [10.1126/science.adg9328](https://doi.org/10.1126/science.adg9328)
- Liu, R.-Y., Rieger, F. M., & Aharonian, F. A. 2017, *ApJ*, 842, 39, doi: [10.3847/1538-4357/aa7410](https://doi.org/10.3847/1538-4357/aa7410)
- Liu, R.-Y., Zhang, H.-M., & Wang, X.-Y. 2023, *ApJL*, 943, L2, doi: [10.3847/2041-8213/acaf5e](https://doi.org/10.3847/2041-8213/acaf5e)
- Lu, W., Beniamini, P., & McDowell, A. 2020, arXiv e-prints, arXiv:2005.10313, doi: [10.48550/arXiv.2005.10313](https://doi.org/10.48550/arXiv.2005.10313)
- Maselli, A., Melandri, A., Nava, L., et al. 2014, *Science*, 343, 48, doi: [10.1126/science.1242279](https://doi.org/10.1126/science.1242279)
- Mimica, P., & Giannios, D. 2011, *MNRAS*, 418, 583, doi: [10.1111/j.1365-2966.2011.19507.x](https://doi.org/10.1111/j.1365-2966.2011.19507.x)
- Nakar, E., Ando, S., & Sari, R. 2009, *ApJ*, 703, 675, doi: [10.1088/0004-637X/703/1/675](https://doi.org/10.1088/0004-637X/703/1/675)
- O'Connor, B., Troja, E., Ryan, G., et al. 2023, *Science Advances*, 9, eadi1405, doi: [10.1126/sciadv.adi1405](https://doi.org/10.1126/sciadv.adi1405)
- Panaitescu, A., & Kumar, P. 2000, *ApJ*, 543, 66, doi: [10.1086/317090](https://doi.org/10.1086/317090)
- Pe'er, A. 2012, *ApJL*, 752, L8, doi: [10.1088/2041-8205/752/1/L8](https://doi.org/10.1088/2041-8205/752/1/L8)
- Ren, J., Wang, Y., Zhang, L.-L., & Dai, Z.-G. 2023, *ApJ*, 947, 53, doi: [10.3847/1538-4357/acc57d](https://doi.org/10.3847/1538-4357/acc57d)
- Rieger, F. M., & Duffy, P. 2022, *ApJ*, 933, 149, doi: [10.3847/1538-4357/ac729c](https://doi.org/10.3847/1538-4357/ac729c)
- Rossi, E., Lazzati, D., & Rees, M. J. 2002, *MNRAS*, 332, 945, doi: [10.1046/j.1365-8711.2002.05363.x](https://doi.org/10.1046/j.1365-8711.2002.05363.x)
- Sari, R., & Esin, A. A. 2001, *ApJ*, 548, 787, doi: [10.1086/319003](https://doi.org/10.1086/319003)
- Sato, Y., Murase, K., Ohira, Y., & Yamazaki, R. 2023, *MNRAS*, 522, L56, doi: [10.1093/mnrasl/slاد038](https://doi.org/10.1093/mnrasl/slاد038)
- Schlaflly, E. F., & Finkbeiner, D. P. 2011, *ApJ*, 737, 103, doi: [10.1088/0004-637X/737/2/103](https://doi.org/10.1088/0004-637X/737/2/103)
- Sironi, L., Keshet, U., & Lemoine, M. 2015, *SSRv*, 191, 519, doi: [10.1007/s11214-015-0181-8](https://doi.org/10.1007/s11214-015-0181-8)
- Sironi, L., Spitkovsky, A., & Arons, J. 2013, *ApJ*, 771, 54, doi: [10.1088/0004-637X/771/1/54](https://doi.org/10.1088/0004-637X/771/1/54)
- Spitkovsky, A. 2008, *ApJL*, 682, L5, doi: [10.1086/590248](https://doi.org/10.1086/590248)
- Srinivasaragavan, G. P., O'Connor, B., Cenko, S. B., et al. 2023, *ApJL*, 949, L39, doi: [10.3847/2041-8213/accf97](https://doi.org/10.3847/2041-8213/accf97)
- Takahashi, K., Ioka, K., Ohira, Y., & van Eerten, H. J. 2022, *MNRAS*, 517, 5541, doi: [10.1093/mnras/stac3022](https://doi.org/10.1093/mnras/stac3022)
- Wang, X.-Y., Liu, R.-Y., & Lemoine, M. 2013, *ApJL*, 771, L33, doi: [10.1088/2041-8205/771/2/L33](https://doi.org/10.1088/2041-8205/771/2/L33)
- Williams, M. A., Kennea, J. A., Dichiara, S., et al. 2023, *ApJL*, 946, L24, doi: [10.3847/2041-8213/acbcd1](https://doi.org/10.3847/2041-8213/acbcd1)
- Yang, J., Zhao, X.-H., Yan, Z., et al. 2023, *ApJL*, 947, L11, doi: [10.3847/2041-8213/acc84b](https://doi.org/10.3847/2041-8213/acc84b)
- Yoon, S. C., Langer, N., & Norman, C. 2006, *A&A*, 460, 199, doi: [10.1051/0004-6361:20065912](https://doi.org/10.1051/0004-6361:20065912)
- Zhang, B., & Mészáros, P. 2002, *ApJ*, 571, 876, doi: [10.1086/339981](https://doi.org/10.1086/339981)
- Zhang, B., Wang, X.-Y., & Zheng, J.-H. 2024, *Journal of High Energy Astrophysics*, 41, 42, doi: [10.1016/j.jheap.2024.01.002](https://doi.org/10.1016/j.jheap.2024.01.002)
- Zhang, B. T., Murase, K., Ioka, K., et al. 2023, *ApJL*, 947, L14, doi: [10.3847/2041-8213/acc79f](https://doi.org/10.3847/2041-8213/acc79f)
- Zou, Y. C., Wu, X. F., & Dai, Z. G. 2005, *MNRAS*, 363, 93, doi: [10.1111/j.1365-2966.2005.09411.x](https://doi.org/10.1111/j.1365-2966.2005.09411.x)